Channel Modelling for Light Communications: Validation of Ray Tracing by Measurements

Hossien B. Eldeeb*, Murat Uysal*, Sreelal Maravanchery Mana†, Peter Hellwig†, Jonas Hilt†, and Volker Jungnickel†

*Department of Electrical and Electronics Engineering, Ozyegin University, Istanbul, Turkey, 34794.

†Photonic Networks and Systems, Fraunhofer Heinrich Hertz Institute, Einsteinufer 37, 10587 Berlin, Germany.

E-mail: hossien.eldeeb@ozyegin.edu.tr, sreelal.maravanchery@hhi.fraunhofer.de

***Abstract*—Light communications, also denoted as LiFi, is promising for future wireless indoor networks. For performance evaluation, the IEEE P802.15.13 and P802.11bb standardization groups agreed upon channel models based on non-sequential ray tracing. In this paper, we validate the modeling approach behind by means of measurements. The same indoor scenarios, where measurements took place in 200 MHz bandwidth, have been modeled in 3D and applying ray tracing. We show that the mean-square error between simulation and measurement is below 2%. Finally, we investigate important channel parameters like path loss and coherence bandwidth as a function of distance with and without line-of-sight.**

***Index Terms*—Light communications, optical wireless communications, channel modeling, ray tracing, channel measurements**

I. Introduction

Nowadays, light communication (LC) technology is gaining more interest due to its huge available bandwidth in unregulated optical spectrum. Both visible light (VL) and infrared (IR) wavelengths can be utilized to design LC systems which can be positioned as either alternative or complementary to radio communications [1], [2]. For example, it is often proposed that visible light communication (VLC) can be used to offload downlink traffic [3]. It is also possible to achieve wireless connectivity in both directions [4] where near-IR is typically used in the uplink [5].

One main research topic in LC is channel characterization which is considered as an essential and precursory stage to evaluate the communication system design [1]. Generally, there are two ways to characterize LC channels. The first one is based on the simulation while the second uses experimental measurements. While simulations can be reproduced on every personal computer, measurements are time-consuming, costly and specific for the particular measured scenario. While simulations are more generic, they have to be validated at least once against measurements in a real scenario.

Simulation methodologies for LC channel modeling can be classified into two major approaches, i.e, deterministic [6]–[11] and stochastic methods [12]–[15]. Recursive calculation [6]–[9] and geometric-based models [10], [11] are the most widely used deterministic techniques, but are typically limited to simple geometries due to computational complexity. As a more flexible alternative to deterministic methods, non-sequential ray tracing can be employed [14], [15]. This stochastic approach allows for the evaluation of the impulse response for environments with complex geometries especially when a large number of reflections are considered. In a ray tracing study, the objects hit by the rays are defined by their physical properties and orientation towards the directions of rays. This allows the ray to be launched and then hit whatever object is in its path. As a result, the ray may be reflected, scattered, refracted, diffracted, or split into sub-rays.

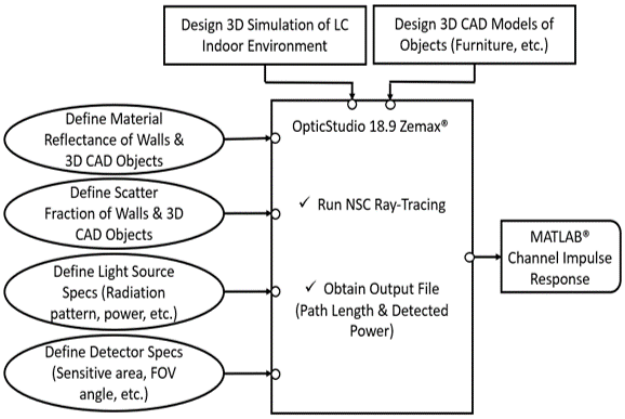

Fig. 1. LC simulation steps

Ray tracing studies were reported for both IR and VL wavelengths [14]–[18]. In [18], advanced non-sequential ray tracing capabilities of optical design software OpticStudio® [19] from Zemax were used to obtain CIRs for various indoor environments with different shapes and sizes. This approach allows the integration of any realistic light source radiation pattern and can handle a large number of reflections (more than 10) for better accuracy. Wavelength-dependent reflectance of surface coating for each material in the environment, which is particularly important at VL wavelengths, as well as different types of reflections (specular, diffuse or mixed) can be further taken into account for a precise characterization. VLC channel models developed through this approach were also adopted as reference channel models in IEEE 802.15.13 and IEEE 802.11bb [20], [21].

Experimental measurements on LC channels are more sporadically reported in the literature [1]. In [22], the dynamic behaviour of LC channels is reported by gathering the data

This work has been supported by H2020 Marie Sklodowska-Curie Innovative Training Network (ITN-VisIoN) under Grant 764461. The work of Murat Uysal has been supported by the Turkish Scientific and Research Council (TUBITAK) under Grant 215E311.

from different room configurations where a network analyzer with a bandwidth between 150 KHz to 38.15 MHz has been utilized. In an effort to validate a spherical model for the diffuse light propagation in a room, the authors in [11] carried out similar measurements with 300 MHz bandwidth. Results indicate that well-known formulas for the integrated sphere can be adapted to model basic properties of diffuse light propagation in a room. Starting from average reflectivity, receiver area and room size, one can compute the path loss and the channel delay spread. Other contributions highlighted the effect of receiver rotation, see [23]. The change of the path loss due to the receiver rotation has been reported to follow a Gamma distribution.

In fact, experimental measurements are time consuming and require dedicated hardware and costly equipment. Therefore, the challenge is to characterize LC channels with a realistic simulation methodology in away to reach a satisfactory matching between simulations and measurements. Afterwards, modelling of more complex scenarios becomes readily accessible. Towards this main objective, in this paper, we carry out measurements and simulations in the same scenarios to validate the approach in [18] which is also the basis of IEEE reference channel models [20], [21]. Our measurement system exploits multiple IR LEDs and photodiodes at both transmitter (Tx) and receiver (Rx) sides and the latest wideband optical front-ends made at Fraunhofer Heinrich Hertz Institute (HHI) and a standard vector network analyser (VNA). In the simulation study, we utilize the same set-up, i.e., the radiation pattern of LEDs, the effect of the receiver directivity, wavelength-dependent reflectance of the walls and objects inside the room, etc. to allow one-to-one comparisons with measurement campaign.

The remainder of the paper is organized as follows. In Section II, we present the ray tracing methodology adopted in our study. In Section III, we explain the measurement methodology and LC scenarios under consideration. In Section IV, we present and compare the results of simulations and measurements. Finally, we conclude in Section V

II. Simulation Methodology

In this section, we briefly summarize the ray tracing approach in [18]. Major steps of this approach are provided in Fig.1. We first create the 3D simulation model of the test environment under consideration in OpticStudio® and import the CAD models of the objects (i.e., furniture, human beings, etc). The coating materials of such CAD objects are defined in the simulation platform where the wavelength-dependent reflectance as well scatter fraction can be specified. After that, the light source specifications such as optical power, radiation pattern, orientations, and number of emitted rays are defined. Additionally, the specifications of the detector such as the sensitive area, field-of-view (FOV) angle, orientations, and directivity are defined.

After the 3D simulation model is created, non-sequential ray tracing is performed to generate an output file containing information about the path length and the power of each ray emitted from the light source (Tx) and arrived to the detector

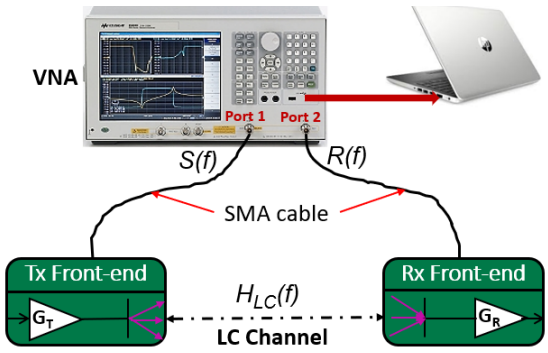

Fig. 2. Channel measurement set-up

(Rx). By processing this information in Matlab®, we can construct the CIR by

$$h(t) = \sum_{i=1}^{N} P_i \delta(t - \tau_i) \tag{1}$$

where N is the number of rays received by the photodetector (PD) and δ is the Dirac delta function. Here, P_i and τ_i respectively denote the power and the propagation delay of the i^{th} ray received by the PD, $i = 1, \cdots, N$.

After obtaining the CIR, various channel parameters can be calculated. One of the important parameters is path loss, which is critical for link budget calculations. With $H_0 = \int_0^\infty h(t)dt$ being the DC channel gain, the path loss can be described as

$$PL = -10 \log_{10}(H_0) \tag{2}$$

Since multiple copies of the signal reach at the receiver through different paths, each of them has a different power level and path length. Hence, the channel is affected by temporal dispersion. The impact of multi-path dispersion is often characterized by the root mean square (RMS) delay spread which can be computed by

$$\tau_{rms} = \sqrt{\frac{\int_0^\infty (t - \mu_\tau)^2 h(t)^2 dt}{\int_0^\infty h(t)^2 dt}} \tag{3}$$

where μ_τ is the mean excess delay. It is well known that higher the value of RMS delay spread, lower is the data transmission rate. Another important parameter is the channel coherence bandwidth, B_c. Assuming a correlation level of 50% [1], the channel coherence bandwidth can be given by $B_{c,50\%} = 1/5\tau_{rms}$.

III. Measurement System and LC Scenarios

A. Measurement System

The channel measurement system (see Fig. 2) is based on frequency sweep technique using a standard Agilent two-port VNA (E5061B-3L5 model), capable of operating between 5 Hz and 3 GHz. At first, a 0 dB continuous-sinusoidal-signal, swept from 1 MHz to 200 MHz in steps of 200 kHz, is delivered to the optical Tx front-end. Then, Tx (consisting of multiple LEDs) radiates the signals through the propagation channel. A large amount of transmitted rays will be captured at the PD array of Rx kept at a particular configuration according to the effective sensitive area and FOV angle of the PD.

Fig. 3. Meeting room where LC measurements were conducted [25].

Table I
Measurement and Simulation Parameters

Parameter	Value
Transmitter Model	OSRAM-OSLON-Black SFH4715AS
Center Wavelength	850 nm
Optical Power	1.3 W
Number of LEDs	4
Receiver Model	HAMAMATSU-S6968 Series
Detector Active Area	150 mm^2
Sensitivity at 850 nm	0.63 A/W
Number of Detectors	5
Room Dimensions	5.7 m$\times$ 4.5 m$\times$ 3 m
Reflection Coefficient	Wall 0.83, Ceiling 0.83, Floor 0.3

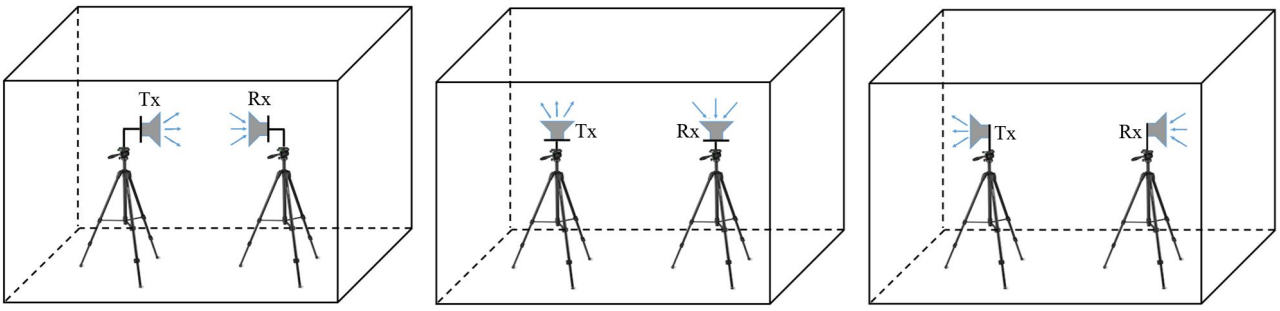

(a) (b) (c)

Fig. 4. LC scenarios under consideration: (a) scenario I, (b) scenario II, (c) scenario III

In our set-up, the Tx front-end consists of four OSRAM OSLON SFH-4715AS LEDs which has the centroid wavelength at 850 nm [24]. Rx front-end is equipped with five HAMAMATSU-S6968 PDs with a high sensitivity around 850 nm. This combination of Tx and Rx arrays maximize the number of captured rays at the Rx which is critical during NLOS scenarios.

The amplitude and phase of the received signal at the port 2 of VNA are compared with the transmitted ones and the corresponding frequency response of the LC system is generated. In this 50 Ohm S-parameter test of VNA, the resultant response consists of frequency response of LC channel, Tx and Rx front-ends. The effect of these front-end responses must be nullified then in order to characterize the LC channel.

Let $S(f)$ denote the transmitted signal. After the propagation through the channel, the received signal is represented as

$$R(f) = H_{LC}(f)H_{sys}(f)S(f) \tag{4}$$

where $H_{LC}(f)$ is frequency response of the LC channel and $H_{sys}(f)$ represents the frequency response of the front-ends. Hence, to obtain the frequency response of the propagation channel, a LOS calibration at a reference distance, d_{ref} is required. The received signal at d_{ref} is given by

$$R_{d_{ref}}(f) = H_{d_{ref}}(f)H_{sys}(f)S(f) \tag{5}$$

where $H_{d_{ref}}(f)$ represents frequency response of the reference LC channel. The calibrated frequency response of the LC channel, is calculated by dividing the received frequency response at any particular distance (denoted by d) by the received frequency response at the reference distance. The resultant normalized frequency response of the channel is given by

$$H_N(f) = \frac{R(f)}{R_{d_{ref}}(f)} = \frac{H_{LC}(f)}{H_{d_{ref}}(f)} \tag{6}$$

From this frequency response, a normalized CIR (denoted by $h_N(t)$) can be calculated using the inverse discrete Fourier transformation method. By integrating $h_N(t)$ over the time, the DC channel gain $H_N(0)$ is calculated. Similarly, we can consider the amplitude value at the lowest frequency as the electrical DC channel gain. Finally, other parameters such as channel path loss, RMS delay-spread and average delay spread can be calculated using (2) and (3).

B. LC Scenarios Under Consideration

As illustrated in Fig. 3, we performed the measurements in a small meeting room at HHI with a dimension of 5.7 m$\times$ 4.5 m$\times$ 3 m. Both Tx and Rx front-ends are deployed on a metal tripod at a height of 1.5 m and with a separation distance of d. In the measurements, three LC scenarios (See Fig. 4) are considered as follows:

- **Scenario I (LOS scenario):** Tx and Rx are facing each other to maintain a LOS link.
- **Scenario II (NLOS with dominant first order reflection):** Tx and Rx face towards the ceiling. The Rx in this case can capture the rays after the reflection, mostly from the ceiling which represents the first-order reflection rays.

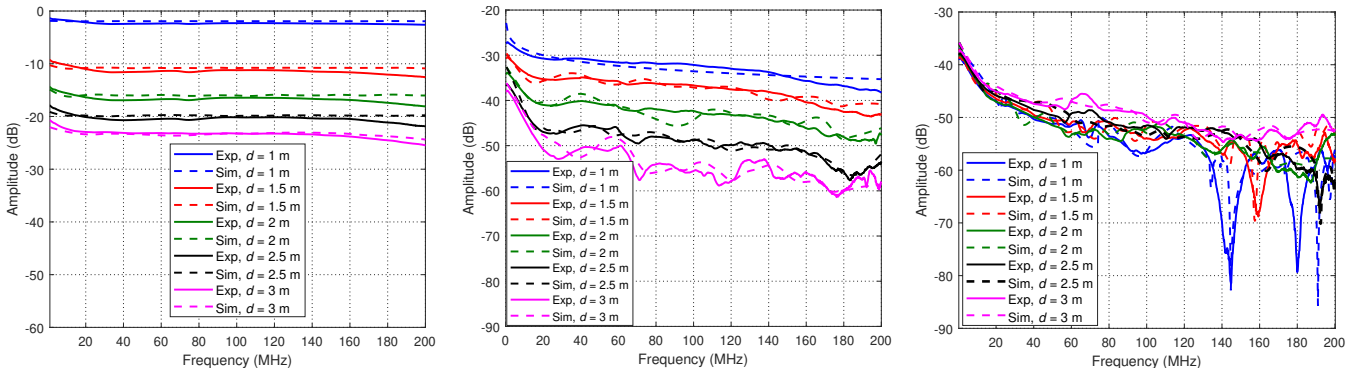

(a) (b) (c)

Fig. 5. Amplitude responses: (a) scenario I, (b) scenario II, (c) scenario III

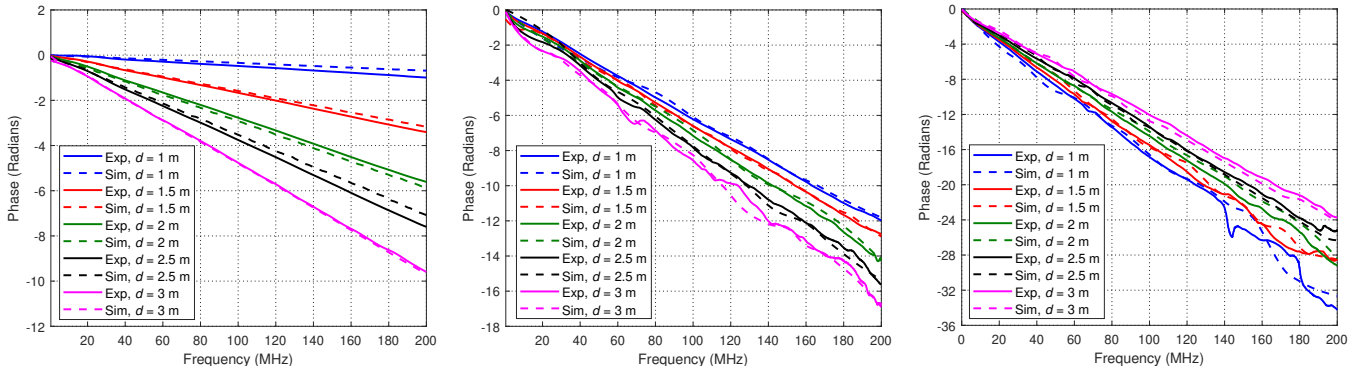

(a) (b) (c)

Fig. 6. Phase responses: (a) scenario I, (b) scenario II, (c) scenario III

- **Scenario III (NLOS with high order reflections):** Tx and Rx face opposite directions. Hence the signalling takes place through the multiple reflections from the surfaces.

For all scenarios under consideration, the value of d varies between 1 m and 3 m with 0.5 m step size.

IV. Results and Discussion

In this section, we present the simulation and experimental results of LC channel characteristics. First, the frequency sweep experiment is performed considering the three main scenarios detailed in the previous section. Then ray tracing simulation is executed by considering the same experimental scenarios.

In the measurement campaign, the calibrated CIR was obtained by keeping the Tx and Rx at a reference distance of d_{ref}=0.8 m [25]. Since the maximum frequency in our measurement is 200 MHz, the time resolution of the simulated CIR was selected as $\frac{1}{2\times\ 200\ MHz} = 2.5\ ns$. Table I provides all simulation and measurement parameters.

Figs. 5 and 6 show the amplitude and phase responses of LC channels obtained for three different scenarios under consideration. In scenario I, where the LOS path is dominant, it is observed that the amplitude response is relatively constant over all bandwidth. As the separation distance between Tx and Rx, increases from 1 m to 3 m, the DC gain of the LC channel reduces. Specifically, a reduction of around 20 dB is noted from 1 m to 3 m distance, which is consistent with the expected $\frac{1}{d^4}$ behaviour.

In the scenario II, where both Tx and Rx face towards the ceiling, the dominant contribution comes from the first reflection path. As the separation distance increases, the overlap between Tx radiation and Rx FOV reduces. Thus the possibility of signaling due to first reflection continues to decline and multi-path reflections get larger. As a result, a drop in the amplitude response is observed which is clearer at frequencies below 20 MHz [6], [11]. For small values of the distance, the amplitude responses at higher frequencies are almost flat. As we increase distance, more ripples becomes visible. This is due to the significant delays of the second and third order reflections, compared to the first one. While being similar in amplitude, phase may be constructive or destructive at some frequencies depending on the power and path length of these superimposed received signals.

In Scenario III, the channel frequency response is dominated by multipath effects since neither the LOS nor the first reflection links are available. Here the diffuse signal characteristics can significantly affect the amplitude and phase response of the channel. The fast drop below 20 MHZ is followed by ripple as well as deep fades especially at frequencies higher than 100 MHz. The position of these fades is very sensitive with respect to the position and direction of Tx and Rx in the room. In all phase response results given in Fig. 6, the slope of the phase response is almost constant if there is minor ripple or fading. But in case of ripple and particularly for the fading events, there is a significant variation in the slope of the phase response.

Fig. 7 presents estimated CIRs from the measurement and

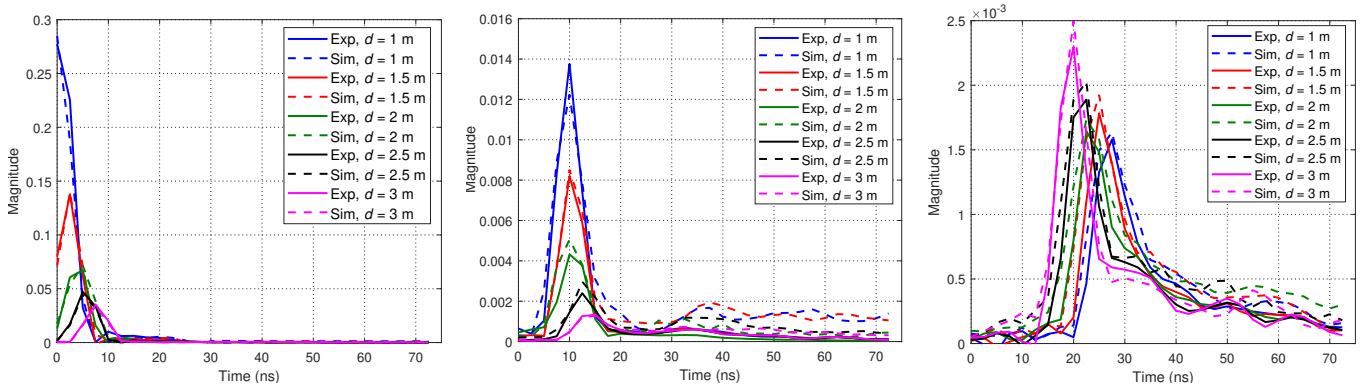

(a) (b) (c)

Fig. 7. CIRs at different separation distances: (a) scenario I (b) scenario II (c) scenario III

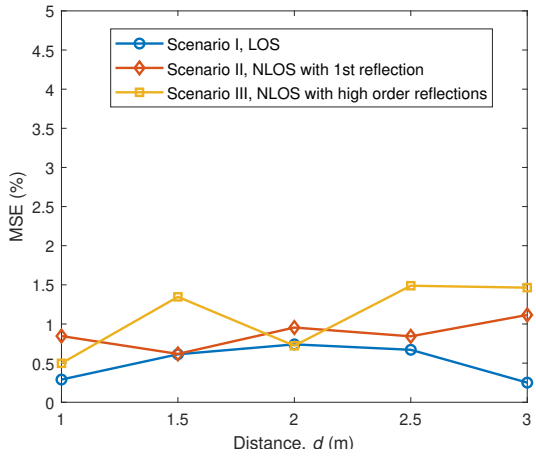

Fig. 8. MSE versus distance for all scenarios under consideration

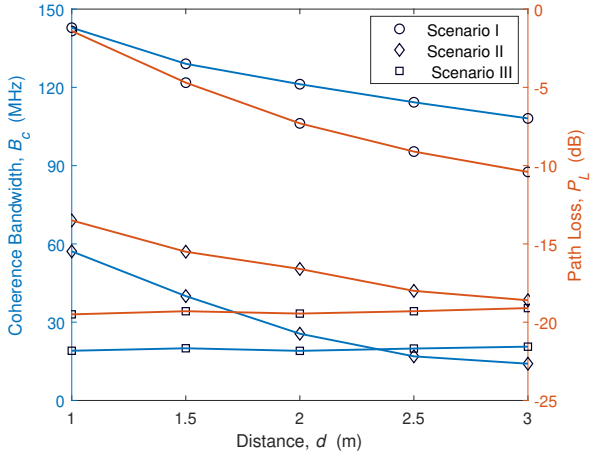

Fig. 9. Path loss and coherence bandwidth of scenarios under consideration

simulation data for the considered scenarios. In Fig. 7(a), due to strong LOS links, only a single peak is observable. In Fig. 7(b) and (c), due to the multiple reflections, the CIR broadens in time domain and the area under the curve gets smaller. In all cases, the strongest peak in the CIR is shifted in time as the path length between Tx and Rx increases. For example, at d = 2 m, the peak values of CIR in scenario I, II, and III lie at 5 ns, 10 ns, and 22.5 ns, respectively. Here, the strongest peak of CIRs is observed at the same point in the experimental and simulated data.

From the above frequency responses and CIRs, it can be concluded that results from simulation and experiments exhibit similar behaviour with having a deviation of 1-3 dB in amplitude and 1-4 radians in phase. The deviation between measurements and simulations partly depends on the fact that reflection coefficients of walls and objects inside the test room could not be measured and representative values were assumed in the simulations.

In order to quantify the accuracy of the simulation results with respect to the measurements further, Fig. 8 presents the mean square error (MSE) between the measurement and simulation data. It can be checked from Fig. 8 that the maximum error percentages are about 0.7%, 1%, and 1.5% for scenario I, II, and III, respectively.

Finally, Fig. 9 presents the path loss and coherence bandwidth of LC channels at all scenarios under consideration. It can be observed that in the presence of LOS transmission (Scenario I) or first order reflections (Scenario II), the path loss decreases when the distance increases. For example, the recorded path loss values at d = 1 m are -1.4 dB and -13.5 dB for scenario I and scenario II, respectively. These reduce to -10.4 dB and -18.6 dB at d = 3 m, respectively for scenario I and scenario II which quantifies the additional path loss when losing the LOS and the first-order reflection. On the other side, when the contribution is mainly based on the high-order reflections as in scenario III, impact of distance on the path loss becomes negligible. It is well known that the diffuse reflection creates a rather constant light distribution in the room. It can be also observed that there is an inverse relationship between the path loss and coherence bandwidth. While the LOS channels (Scenario I) have higher coherence bandwidth and lower path loss, the opposite is true for NLOS channels with high order reflections (Scenario III).

V. Conclusions

In this paper, we have carried out an experimental study to validate LC channel models obtained through non-sequential ray tracing. First, we have conducted CIR measurements in an empty room for different LC scenarios including LOS and NLOS cases. The measurements were based on frequency

sweeping technique using a VNA together with optical front-ends. Then, the same scenarios were modeled in OpticStudio® and non-sequential ray tracing was used to obtain CIRs. Results of both approaches have indicated a very good match in both, frequency and time domains. Moreover, important channel parameters such as path loss and coherence bandwidth were extracted from the results.

REFERENCES

[1] A. Al-Kinani, C.-X. Wang, L. Zhou, and W. Zhang, "Optical wireless communication channel measurements and models," *IEEE Commun. Surveys & Tut.*, vol. 20, no. 3, pp. 1939–1962, 2018.

[2] Z. Ghassemlooy, S. Arnon, M. Uysal, Z. Xu, and J. Cheng, "Emerging optical wireless communications-advances and challenges," *IEEE J. on selected areas in commun.*, vol. 33, no. 9, pp. 1738–1749, 2015.

[3] C. Chen, R. Bian, and H. Haas, "Omnidirectional transmitter and receiver design for wireless infrared uplink transmission in lifi," in *2018 IEEE Int. Conf. on Commun. Workshops (ICC Workshops)*. IEEE, 2018, pp. 1–6.

[4] T. Koonen, F. Gomez-Agis, F. Huijskens, K. A. Mekonnen, Z. Cao, and E. Tangdiongga, "High-capacity optical wireless communication using two-dimensional ir beam steering," *J. of Lightwave Technol.*, vol. 36, no. 19, pp. 4486–4493, 2018.

[5] H. B. Eldeeb, H. A. Selmy, H. M. Elsayed, R. I. Badr, and M. Uysal, "Efficient resource allocation scheme for multi-user hybrid vlc/ir networks," in *2019 IEEE Photonics Conference (IPC)*. IEEE, pp. 1–2.

[6] J. R. Barry, J. M. Kahn, W. J. Krause, E. A. Lee, and D. G. Messerschmitt, "Simulation of multipath impulse response for indoor wireless optical channels," *IEEE J. on selected areas in commun.*, vol. 11, no. 3, pp. 367–379, 1993.

[7] F. Lopez-Hermandez and M. Betancor, "Dustin: algorithm for calculation of impulse response on ir wireless indoor channels," *Electronics Lett.*, vol. 33, no. 21, pp. 1804–1806, 1997.

[8] J. B. Carruthers and P. Kannan, "Iterative site-based modeling for wireless infrared channels," *IEEE Trans. Antennas and Propagation*, vol. 50, no. 5, pp. 759–765, 2002.

[9] K. Lee, H. Park, and J. R. Barry, "Indoor channel characteristics for visible light communications," *IEEE communications letters*, vol. 15, no. 2, pp. 217–219, 2011.

[10] J. B. Carruthers and J. M. Kahn, "Modeling of nondirected wireless infrared channels," *IEEE trans. commun.*, vol. 45, no. 10, pp. 1260–1268, 1997.

[11] V. Jungnickel, V. Pohl, S. Nonnig, and C. Von Helmolt, "A physical model of the wireless infrared communication channel," *IEEE J. Selected Areas in Commun.*, vol. 20, no. 3, pp. 631–640, 2002.

[12] N. Hayasaka and T. Ito, "Channel modeling of nondirected wireless infrared indoor diffuse link," *Electronics and Communications in Japan (Part I: Communications)*, vol. 90, no. 6, pp. 9–19, 2007.

[13] V. Pohl, V. Jungnickel, and C. Von Helmolt, "Integrating-sphere diffuser for wireless infrared communication," *IEE Proceedings-Optoelectronics*, vol. 147, no. 4, pp. 281–285, 2000.

[14] O. González, S. Rodríguez, R. Pérez-Jiménez, B. R. Mendoza, and A. Ayala, "Error analysis of the simulated impulse response on indoor wireless optical channels using a monte carlo-based ray-tracing algorithm," *IEEE Trans. Commun.*, vol. 53, no. 1, pp. 124–130, 2005.

[15] M. S. Chowdhury, W. Zhang, and M. Kavehrad, "Combined deterministic and modified monte carlo method for calculating impulse responses of indoor optical wireless channels," *J. of Lightwave Technol.*, vol. 32, no. 18, pp. 3132–3148, 2014.

[16] S. Dimitrov, R. Mesleh, H. Haas, M. Cappitelli, M. Olbert, and E. Bassow, "On the sir of a cellular infrared optical wireless system for an aircraft," *IEEE Journal on Selected Areas in Communications*, vol. 27, no. 9, pp. 1623–1638, 2009.

[17] O. González, S. Rodríguez, R. Pérez-Jiménez, B. R. Mendoza, and A. Ayala, "Comparison of monte carlo ray-tracing and photon-tracing methods for calculation of the impulse response on indoor wireless optical channels," *Optics express*, vol. 19, no. 3, pp. 1997–2005, 2011.

[18] F. Miramirkhani and M. Uysal, "Channel modeling and characterization for visible light communications," *IEEE Photon. J.*, vol. 7, no. 6, pp. 1–16, 2015.

[19] Zemax., https://www.zemax.com/, [Accessed: May 26, 2020].

[20] M. Uysal, F. Miramirkhani, O. Narmanlioglu, T. Baykas, and E. Panayirci, "IEEE 802.15. 7r1 reference channel models for visible light communications," *IEEE Commun. Mag.*, vol. 55, no. 1, pp. 212–217, 2017.

[21] M. Uysal, F. Miramirkhani, T. Baykas, N. Serafimovski, and V. Jungnickel, "IEEE 802.11 bb reference channel models for indoor environments," doc: IEEE 11-18-1236-01-00bb, July, 2018.

[22] H. Hashemi, G. Yun, M. Kavehrad, and F. Behbahani, "Frequency response measurements of the wireless indoor channel at infrared frequencies," in *Proceedings of ICC/SUPERCOMM'94-1994 Int. Conf. on Commun.* IEEE, 1994, pp. 1511–1515.

[23] M. R. Pakravan and M. Kavehrad, "Indoor wireless infrared channel characterization by measurements," *IEEE Trans. Veh. Technol.*, vol. 50, no. 4, pp. 1053–1073, 2001.

[24] OSRAM., https://www.osram.com/os/ecat/OSLUX, [Accessed: May 26, 2020].

[25] S. M. Mana, P. Hellwig, J. Hilt, P. W. Berenguer, and V. Jungnickel, "Experiments in non-line-of-sight li-fi channels," in *2019 Global LIFI Congress (GLC)*. IEEE, 2019, pp. 1–6.